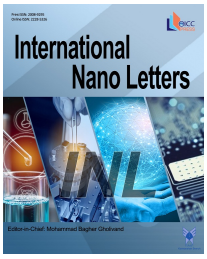

Volume 14, Issue 3, 142412 (1-11)

International Nano Letters (INL)

https://doi.org/10.57647/inl.2024.1403.12

Effect of Ni-Doping on the Structural and Optical Properties of ZnO Nanoparticles by Sol-Gel Method

Elahe Moeini Sede[1,2], Mohammad Hossein Majles Ara[1,2,*], Seyedeh Soraya Mousavi[1,3], Fereshteh Rasouli Asl[4]

[1]*Nanophysics Lab, Faculty of Physics, Kharazmi University, Tehran, Iran.*
[2]*Applied Science Research Center, Kharazmi University, Tehran, Iran.*
[3]*Department of Physics, Faculty of Physics and Chemistry, Alzahra University, Tehran, Iran.*
[4]*Catalysts and Organic Synthesis Research Laboratory, Department of Chemistry, Iran University of Science and Technology, Tehran, Iran.*

[*]**Corresponding author:** majlesara@gmail.com

Original Research

Abstract:

In this study, the structure of zinc oxide doped with nickel at different concentrations of 0%, 1%, 3%, 5%, and 10% was examined. Zinc oxide was synthesized using the sol-gel method. Prepared sols coated on silicon wafer by spin coating method to be used as a photodiode in an electrical circuit for evaluation. XRD, UV-Vis, FT-IR, and SEM analyses were utilized to compare the structures of the solutions, powders and thin layers. The zinc oxide structure, with the addition of nickel, reduced in size from 28 nm to 21 nm. The substituted nickel created defects, which led to peak broadening of XRD and a blue shift in UV-Vis spectrum. The photovoltaic properties are studied to understand the behavior of the structures and the current-voltage diagrams of the samples were plotted. The calculations indicate that the zinc oxide sample doped with 3% nickel, prepared using this method, exhibits the best performance as an optical photodiode in the UV range. It shows a better response in I-C curve and ideality factor. Also, the structure of this percentage has the best performance.

Keywords:

Zinc oxide; Nickel doping; NZO nanoparticles; Photodiodes; P-N junctions

Cite this article: Moeini Sede, E., Majles Ara, M.H., Mousavi, S.S., Rasouli Asl, F. Effect of Ni-Doping on the Structural and Optical Properties of ZnO Nanoparticles by Sol-Gel Method. *Int. Nano Lett.* **14**(3), 142412 (2024).

1. Introduction

Transition metals (TMs) are defined by their partially filled d subshells and play a crucial role in bridging the gap between the s-block and p-block elements on the periodic table. This unique positioning endows them with a range of distinctive chemical and physical properties, such as variable oxidation states and the ability to form complex coordination compounds. However, a contentious issue arises concerning the classification of elements located at the boundary between the main group and transition metals, particularly those in Group 12: zinc (Zn), cadmium (Cd), and mercury (Hg). These elements are characterized by having fully filled d sub-shells in their ground states.

Despite having fully filled d subshells, Zn, Cd, and Hg can still form cations with incomplete d sub-shells, which complicates their classification within the transition metals. The behavior of these elements deviates from that of traditional transition metals, which typically exhibit a range of oxidation states and significant d-electron involvement in bonding and reactions. For instance, zinc (Zn) is known for its unique properties, including its relatively low reactivity compared to other transition metals and its role in various biochemical processes. The debate surrounding the placement and classification of these elements underscores the complexity of their electronic structures and the need for a nuanced understanding of their chemical behavior. Zinc is a white metal that ranks among the most abundant elements in the Earth's crust. It readily forms zinc oxide (ZnO), a II-VI metal-oxide semiconductor. ZnO is notable for its non-toxic nature and possesses a direct bandgap of approximately 3.4 eV, coupled with a large exciton binding energy of 60 meV. These properties have garnered significant interest in various applications, including gas sensors and ultraviolet (UV) detectors [1–4].

Zinc oxide (ZnO) is notable for its wide bandgap and strong

excitonic effects, which enhance its performance in optoelectronic applications. These properties make ZnO effective in light-emitting devices, piezoelectric sensors, and photocatalysis. Its direct bandgap allows for efficient light emission and absorption, while its high exciton binding energy further boosts its utility in various applications [1–4]. Furthermore, the properties of zinc oxide (ZnO) can be significantly tailored through doping with various transition metals such as nickel (Ni), cobalt (Co), and iron (Fe). Doping introduces a third element into the ZnO lattice, modifying its electronic structure and consequently affecting its physical properties. For example, doping can influence the bandgap, electrical conductivity, optical characteristics, and even impart magnetic properties to the material [2–6].

Among these transition metals, nickel (Ni) is particularly advantageous as a dopant for ZnO. Nickel's unique characteristics make it superior to other transition metals such as cobalt and iron for several reasons. First, nickel is known for its ability to induce substantial changes in the electronic and optical properties of ZnO, including enhancements in photoluminescence and magnetic behavior. Nickel doping can effectively tune the bandgap of ZnO, which is crucial for optimizing its performance in various optoelectronic applications. Moreover, nickel's relatively small ionic radius allows for effective integration into the ZnO lattice, leading to stable and well-defined doping effects. Cobalt can introduce magnetic properties but may lead to increased lattice distortions and less optimal optical performance compared to nickel. Iron, on the other hand, tends to affect the electronic properties in a less controlled manner, potentially leading to increased defect states and reduced material quality. Overall, Ni-doped ZnO presents a compelling choice for advanced technological applications due to its ability to enhance both optical and magnetic properties while maintaining structural stability. This makes nickel-doped ZnO a highly significant material in the field of material science and advanced optoelectronics [3, 5, 7].

There are several established methods for synthesizing doped zinc oxide (ZnO), including chemical vapor deposition (CVD), atomic beam sputtering, solvothermal methods, and the sol-gel technique [8–11]. Each of these methods offers distinct advantages and limitations depending on the desired properties of the final material and the specific application. Chemical vapor deposition (CVD) is a widely used method that involves depositing a thin film of ZnO from vapor phase precursors onto a substrate. While CVD can produce high-quality films with excellent control over thickness and composition, it generally requires high temperatures and expensive equipment, making it less cost-effective for large-scale production. Atomic beam sputtering is another technique where ZnO is deposited onto a substrate using sputtered atoms from a target material. This method can achieve high purity and uniformity in the deposited layers, but it also involves complex apparatus and can be limited by the size of the substrate. Solvothermal methods involve the reaction of zinc precursors in a solvent under high temperature and pressure. This technique allows for the synthesis of ZnO nanoparticles with controlled size and morphology. However, the requirement for high-pressure and temperature conditions can increase operational complexity and cost. The sol-gel method, on the other hand, has garnered significant attention due to its simplicity, cost-effectiveness, and ability to produce high-quality ZnO with controlled properties [12–15].

Although Ni-doped ZnO has been widely studied for structural and optical purposes, there is a lack of systematic studies correlating different Ni-doping levels with the device performance of ZnO/Si photodiodes, especially for low-temperature and low-cost sol–gel derived films. Previous reports have focused mainly on powder properties or thin-film characterization, but do not evaluate how Ni concentration influences the band structure, optical absorption, defect states, and ultimately the I–V characteristics of a real ZnO/Si junction. Therefore, the optimal Ni-doping percentage for photodiode applications remains unclear. In this work, we fill this gap by synthesizing 1–5% Ni-doped ZnO via a sol–gel route, characterizing the material at solution, powder, and thin-film stages, and fabricating a ZnO/Si photodiode to directly determine the doping level that yields the best device performance [16–18].

In this study (as shown in Scheme 1), the sol-gel method was used to synthesize nickel-doped zinc oxide (NZO) with nickel concentrations ranging from 0% to 10%. The effects of different doping levels on the structural, optical, and electrical properties of NZO nanoparticles were investigated using this approach. By varying the nickel concentration, a range of desirable properties was achieved, such as a larger bandgap and enhanced UV sensing capabilities, demonstrating the effectiveness of the sol-gel method for tuning ZnO properties for advanced applications. Lithography was employed for layer deposition, and a silicon substrate was used as the cathode, with a silver circuit designed to evaluate the current-voltage characteristics of the circuit.

2. Experimental perosedure

2.1 Materials

The materials used in this process are listed in Table 1.

2.2 Method

1 molar Ni-doped ZnO sols were prepared using high-purity zinc acetate dihydrate and nickel (II) nitrate hexahydrate in precise proportions. First, 20 mL of ethanol was stirred at 50 °C for 2 minutes. Triethylamine served as the solvent and stabilizer. The molar ratio of trimethylamine to zinc acetate dehydrate was adjusted to 2:5. After adding trimethylamine, the solution was stirred for 5 minutes. In the sol-gel process, zinc acetate dihydrate was dissolved in a mixture of ethanol and triethylamine at room temperature. This solution was stirred for 30 minutes to produce a clear, homogeneous, and transparent sol, which represented the ZnO.

For doping, nickel (II) nitrate hexahydrate was added to the sol in molar ratios of 1%, 3%, 5%, and 10% nickel, followed by stirring for an additional 15 minutes. The result was a greenish, clear, and homogeneous solution.

Nano powders and thin layers were then prepared from this sol. The nano powders were obtained by allowing the sol to stand for 72 hours, during which crystals formed. These

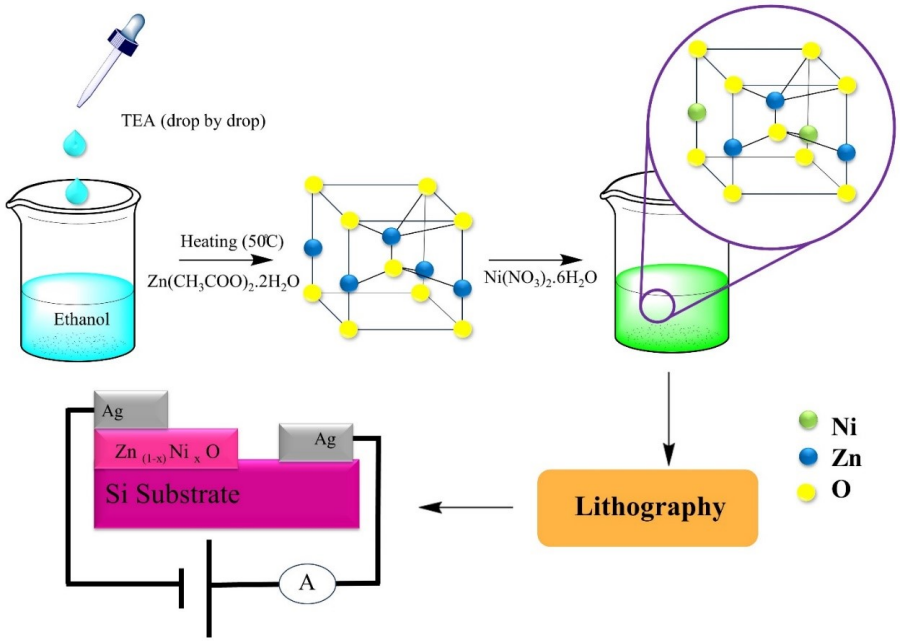

Scheme 1. Overall view of this project.

powders were dried in an oven at 120 °C to evaporate the solvent, and then calcined in a furnace at 400 °C for 2 hours to finalize the material.

Thin films were deposited on glass substrates and Si substrates, which were pre-cleaned using the RCA method, from $Zn_{1-x}Ni_xO$ sols with doping concentrations of x = 0, 1%, 3%, 5%, and 10%. The spin coating parameters were as follows: step 1: 2000 rpm for 10 seconds. step 2: 3000 rpm for 30 seconds.

Following deposition, the films were annealed at 400 °C for 2 hours. The resulting films consisted of a single layer.

3. Result and discussion

3.1 Characterization

Adding Ni^{2+} ions to the ZnO network structure introduces significant changes. Ni^{2+} ions can integrate into the structure in two distinct ways: they can either occupy interstitial octahedral coordination sites or substitute for $Zn2^{2+}$ ions. The latter substitution is ideal as it provides a free electron (charge carrier), thereby enhancing the electronic properties of ZnO as a host material. However, when Ni^{2+} ions occupy interstitial sites, defects are introduced. These interstitial defects occur when the solubility limit of Ni^{2+} in ZnO is exceeded, leading to the formation of NiO complexes, which results in the separation of the electron charge system. This project indicates that the solubility of Ni^{2+} ions in ZnO using the sol-gel method is approximately 5%. Higher solubility levels of Ni^{2+} in the ZnO network can be achieved using other techniques such as Pulsed Laser Deposition (PLD) [19–22].

3.1.1 XRD

X-ray diffraction (XRD) analysis was employed to investigate the crystalline structure of the synthesized ZnO samples and to understand the impact of Ni^{2+} doping on the ZnO lattice. The XRD pattern of the pure ZnO powder was first obtained and compared against standard reference patterns available in the X'Pert HighScore software. As depicted in figure 1, the pattern exhibited a prominent peak corresponding to the (101) plane, a characteristic peak of ZnO, confirming the purity and crystalline integrity of the ZnO sample. This initial analysis set a baseline for subsequent evaluations of the doped samples [13].

In the next phase of the study, ZnO was doped with Ni^{2+} ions at varying concentrations of 1%, 3%, 5%, and 10%. The XRD patterns of these doped samples were analyzed to observe any structural changes or shifts in peak positions. For the samples with 1% and 3% Ni^{2+} doping, minimal shifts were observed in the XRD peaks, indicating that the Ni^{2+} ions were effectively incorporated into the ZnO lattice with only minor lattice stress. This suggests that up to a 3%

Table 1. Materials.

Name	Chemical formula	Purity	Source
Ethanol	C_2H_6O	99.99%	Merc
Zinc acetate dehydrate	$Zn[C_2H_3O_2]_2 \cdot 2H_2O$	99.99%	Merc
Triethylamine	$N(C_2H_5)$	99.99%	Merc
Nichel nitrate	$Ni[NO_3]_2 \cdot 6H_2O$	99.99%	Merc

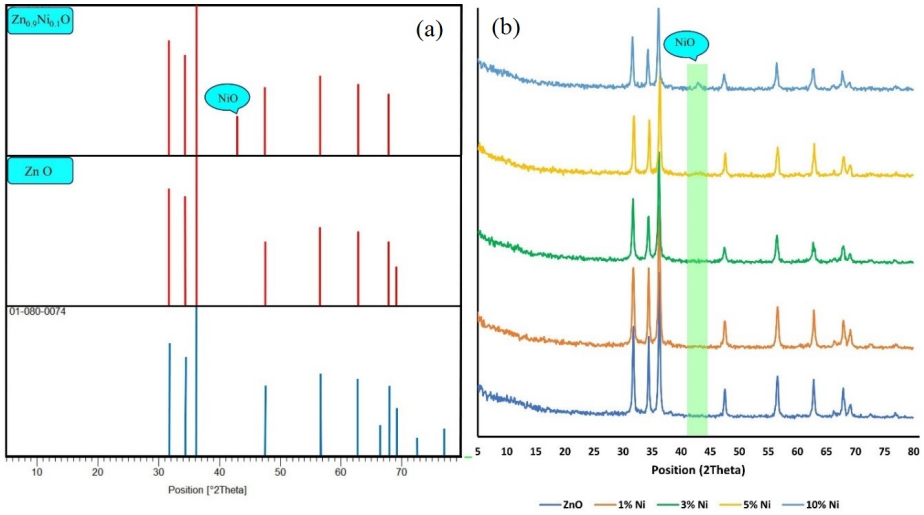

Figure 1. XRD pattern of the structures. (a) Peak position of pure ZnO and $Zn_{0.9}Ni_{0.1}O$ in comparison with PDF card. (b) XRD patterns of ZnO and Ni doped ZnO in different Ni concentration.

concentration, the Ni^{2+} ions substitute for Zn^{2+} ions without significantly disrupting the crystal structure [14–16]. However, when the Ni^{2+} doping concentration was increased to 5%, a weak secondary peak appeared around 43 degrees in the 2θ scan. This peak corresponds to NiO, indicating the onset of a secondary phase. The presence of this NiO peak suggests that the ZnO lattice can no longer accommodate the additional Ni^{2+} ions beyond this concentration, leading to the formation of a separate NiO phase. This finding points to a solubility limit of approximately 5% for Ni^{2+} ions in the ZnO lattice. At higher doping concentrations, specifically 10%, the XRD patterns showed increased lattice stress and more pronounced secondary peaks, confirming that excess Ni^{2+} ions precipitate as NiO due to the limited solubility in the ZnO lattice [19–23].

The XRD analysis conclusively demonstrates that ZnO can be doped with Ni^{2+} ions up to a concentration of 5% without significant phase separation. Beyond this doping concentration, the ZnO lattice experiences structural instability, leading to the formation of secondary NiO phases. This solubility limit is critical for optimizing the doping process to enhance the electronic and structural properties of ZnO for various applications. These findings provide valuable insights into the doping mechanisms and the structural limitations of ZnO when used as a host material for Ni^{2+} ions, which can guide future research and development in this area [24, 25].

Using XRD analysis and X'Pert software, structural data of zinc oxide, such as Miller indices, diffraction angles, sets of crystal planes, and FWHM (Full Width at Half Maximum) of the peaks, can be calculated [26–28].

According to the Scherrer formula, the smaller the FWHM peak width, the larger the crystal size. The obtained data can be observed in Table 2.

Table 2. Characteristics of $Zn_{1-x}Ni_xO$ samples obtained using XRD analysis.

	Hkl	2θ (Degree)	FWHM	Crystal size (nm)
ZnO	100	31.761	0.295	28.623
	002	34.395	0.394	
	101	36.236	0.295	
$Zn_{0.99}Ni_{0.01}O$	100	31.749	0.295	21.430
	002	34.395	0.394	
	101	36.224	0.394	
$Zn_{0.97}Ni_{0.03}O$	100	31.693	0.394	21.427
	002	34.348	0.295	
	101	36.173	0.295	
$Zn_{0.95}Ni_{0.05}O$	100	31.857	0.295	21.436
	002	34.499	0.295	
	101	36.319	0.394	
$Zn_{0.9}Ni_{0.1}O$	100	31.614	0.394	21.428
	002	34.277	0.295	
	101	36.190	0.394	

In the (100) peak, it is observed that the FWHM for zinc oxide doped with 3% and 10% nickel has increased compared to pure zinc oxide. This increase could be due to enhanced internal stress and the introduction of distortions in the lattice caused by the presence of nickel. Additionally, it may indicate a reduction in crystallite size. For the (002) peak, a decrease in FWHM from 0.394 to 0.295 is observed for 3%, 5%, and 10% nickel doping, indicating improved crystal quality along the c-axis. This improvement may be due to better nickel distribution in the structure, reduced internal stress, and enhanced atomic layer ordering. For the (101) peak, FWHM values for 1%, 5%, and 10% nickel doping have increased, reflecting higher defects and stress in this plane. Overall, it can be concluded that $Zn_{0.95}Ni_{0.05}O$ and $Zn_{0.97}Ni_{0.03}O$ exhibit a lower stress structure in these three planes of the hexagonal wurtzite lattice.

Using the Scherer equation, the particle sizes were calculated, and all particles are less than 30 nanometers. Specifically, the particle sizes for 1%, 3%, 5%, and 10% nickel doping in the zinc oxide structure are 28.623, 21.430, 21.427, and 21.428 nanometers, respectively. Overall, the addition of nickel to the structure results in a reduction in particle size, with the smallest sizes observed for 3% and then 10% nickel doping (Table 2).

3.1.2 FT-IR

To confirm the structural integrity of the synthesized ZnO samples doped with various concentrations of Ni^{2+} (0%, 1%, 3%, 5%, and 10%), FT-IR analysis was conducted on all samples. The FT-IR spectra (figure 2) revealed several significant peaks, providing insights into the chemical structure and the presence of specific functional groups within the samples. A broad peak around 3440 cm^{-1} was observed, which can be attributed to the stretching and bending vibrations of OH groups. This peak is likely due to the residual solvent (ethanol) or water from the nickel acetate salt. The presence of these OH groups indicates that the samples have some interaction with moisture, which is a common occurrence in samples synthesized using solution-based methods [25–27].

Another notable peak appeared at approximately 2900 cm^{-1}, corresponding to the C-H stretching vibrations. This peak suggests the presence of organic residues, such as the solvent, acetate groups, or residual TEA (triethanolamine) used during the synthesis. A peak at 2350 cm^{-1} was identified, indicative of CO_2 from the atmosphere, which suggests that carbon dioxide was adsorbed on the sample surface during handling and preparation for FT-IR analysis. Furthermore, a weak peak at 1526 cm^{-1} was observed, which could be due to residual nitrate groups from the nickel nitrate salt used in the doping process. This indicates that not all nitrate groups were eliminated during the synthesis, possibly due to incomplete decomposition or washing. A peak at 1380 cm^{-1} was associated with C=O stretching vibrations, confirming the presence of a small amount of acetate in the structure. This can be attributed to the incomplete removal of acetate groups from the precursor salts during the synthesis. Additionally, a peak at 885 cm^{-1} was identified as belonging to N-H bending vibrations, suggesting the presence of nitrogen-containing groups, possibly from TEA used in the synthesis [29, 30].

Most importantly, a sharp peak at 560 cm^{-1}, characteristic of the ZnO crystal structure, was observed. The intensity and sharpness of this peak varied with the doping concentration. The peak was sharper for the sample doped with 3% Ni^{2+}, indicating a more crystalline structure. In contrast, the peak intensity decreased significantly for $Zn_{0.9}Ni_{0.1}O$ the sample doped with 10% Ni^{2+}, suggesting structural distortion and the possible formation of secondary phases. These findings suggest that $Zn_{0.97}Ni_{0.03}O$ exhibits the best structural integrity among the tested samples, maintaining a crystalline structure with minimal defects. Higher doping concentrations, such as 10% Ni^{2+}, result in significant structural changes and the appearance of secondary phases, indicating the solubility limit of Ni^{2+} in the ZnO lattice. These observations align with the XRD results, further validating the optimal doping concentration for preserving the ZnO network integrity. The combined analysis from FT-IR and XRD confirms that 3% Ni^{2+} doping is ideal for maintaining the structural and chemical stability of the ZnO lattice, while higher doping levels introduce more defects and secondary phases [31, 32].

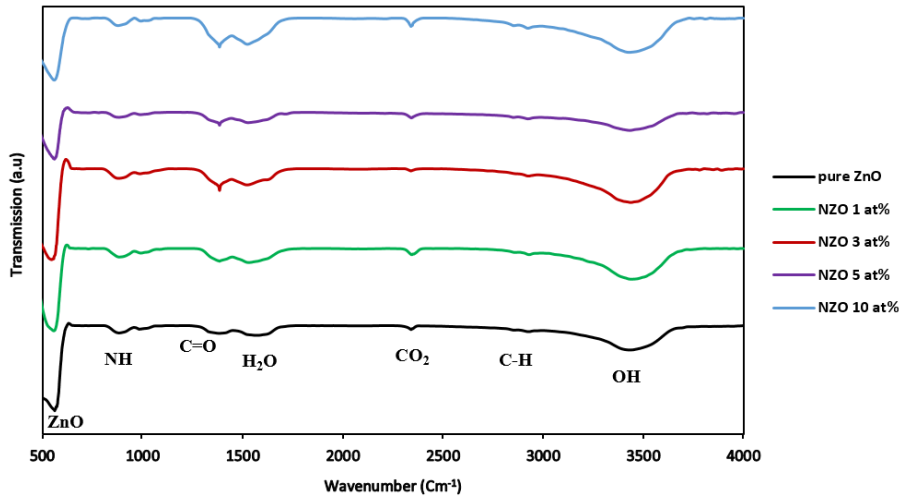

Figure 2. FT-IR spectrum of structural. $Zn_{1-x}Ni_xO$ (X = 0, 1, 3, 5, 10).

3.1.3 UV-Vis

Figure 3 (a) examines the absorption spectra of thin zinc oxide films with various nickel percentages (0, 1, 3, 5 and 10%). The broad peak observed before the main peak (lambda max) in the absorption spectrum of ZnO synthesized via the sol-gel method could be due to structural defects, impurities, quantum size effects from the small particle size, or surface adsorption of molecules. These factors lead to absorption at shorter wavelengths (higher energy), appearing as an additional peak in the spectrum. The lambda max for zinc oxide has been reported as 360 nanometers in studies, and the absorption in this region will be further examined. Clearly, as the percentage of nickel in the ZnO structure increases, the absorption at the maximum point of 360 nm decreases. This suggests that with increasing impurity percentage, the amount of ZnO in the structure decreases [33–35].

As seen in figure 3, with the increase in nickel percentage, the absorption decreases. This could be due to a change in the hexagonal structure of zinc oxide to a different structure. This factor might also explain the results obtained from the XRD analysis. The change in the lattice structure compared to pure zinc oxide in all three Miller indices could represent a significant alteration from the hexagonal structure, which has lower absorption in the maximum wavelength range of zinc. According to the equation:

$$(\alpha h\nu)^2 = B(h\nu - E_g) \tag{1}$$

where $h\nu$ is the photon energy, E_g is the optical bandgap, B is a constant for the semiconductor, and α is the absorption coefficient. If the graph of $(h\nu)^2$ versus photon energy $(h\nu)$ is plotted and its slope calculated, the bandgap of the thin films can be determined [34–37].

If the plot of $\alpha h\nu$ versus energy is drawn, we will observe that the slope of the curves decreases with an increase in nickel content. However, it is also observed that the bandgap increases, resulting in a blue shift in the graph (Fig. 3 b) This increase is due to the bulk NiO structure, which has a bandgap around 4.0 eV (Fig. 3 b), causing the bandgap of zinc oxide with nickel impurities to be larger compared to pure zinc oxide [38–43].

3.1.4 SEM

The SEM images of 1 M zinc oxide powder samples doped with various percentages of nickel are shown in the figure 4 (a-f). As observed, all samples consist of spherical particles with dimensions less than 100 nanometers. These images reveal the uniformity and morphology of the nanoparticles, indicating that the doping process does not significantly alter the shape of the particles. The average size of these nanoparticles is approximately 60 nm, suggesting a consistent particle size across different samples. This uniform size distribution is critical for ensuring predictable and reproducible properties in various applications. More detailed analysis shows that the particle sizes correspond to the doping levels of 1% (Fig. 4 a), 3% (Fig. 4 b), 5% (Fig. 4 c) and 10% (Fig. 4 d) nickel, with an average size of 48 nm. As observed in the figure, the size of the nanoparticles with and without nickel has not changed significantly, and the structure remains constant. This suggests that at this percentage of nickel, the zinc oxide lattice structure is not disrupted. It can be seen that the particle sizes in the zinc oxide nanoparticles are 59, 33, 47, and 36 nm, with the range varying between 30 to 60 nm. However, this could be due to incomplete washing or agglomeration during the synthesis process. According to the XRD analysis, which was shown using the Scherrer equation, the particle size ranges between 21 to 28 nm [29, 43–46].

3.2 Discussion

The structure of zinc oxide can be formed in three ways: wurtzite, which is the most stable crystal structure and hexagonal; zinc blende, which has a cubic structure; and rock salt, which also has a cubic structure. As indicated in the XRD analysis, the characteristic peak at 36 degrees for the (101) plane suggests a hexagonal wurtzite structure. As reviewed in other articles, the electron shells structures of zinc and nickel are respectively as follows:

$$_{30}\mathrm{Zn} : 1S^2/2S^22P^6/3S^23P^6/4S^23d^{10} \tag{2}$$

$$_{28}\mathrm{Ni} : 1S^2/2S^22P^6/3S^23P^6/4S^23d^8 \tag{3}$$

As observed, the nickel atom has a smaller radius compared to the zinc atom, and when it replaces the zinc atom, a sub-

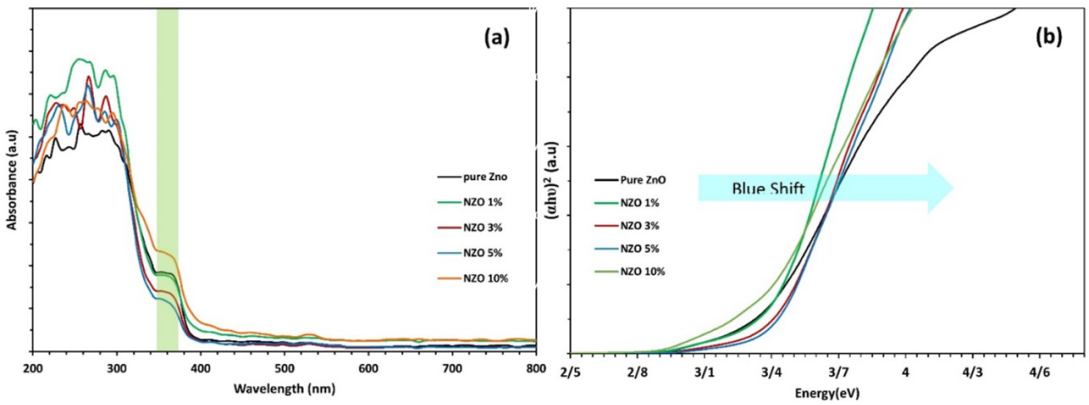

Figure 3. (a) Absorption curve of Pure ZNO, ZNO 1%, ZNO 3%, ZNO 5%, and ZNO 10%. (b) Energy- $\alpha h\nu$ curve of ZNO, ZNO 1%, ZNO 3%, ZNO 5%, and ZNO 10%.

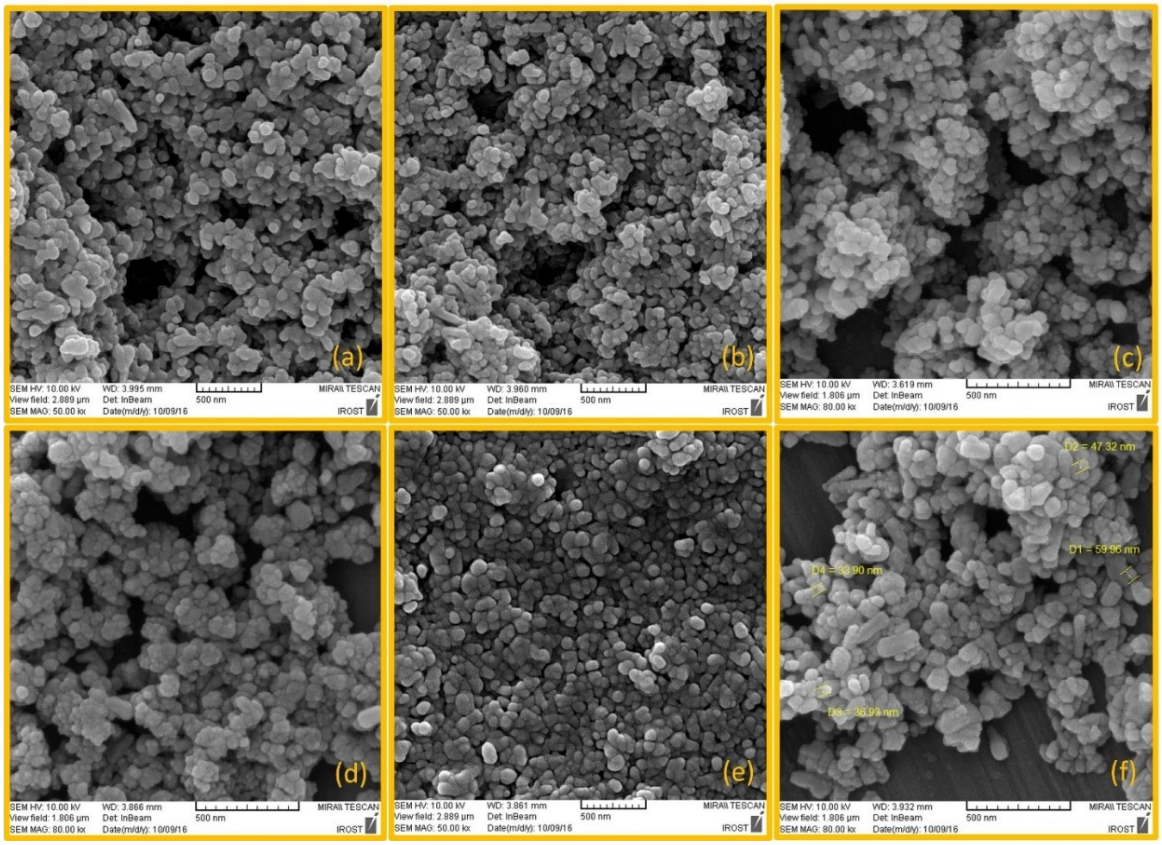

Figure 4. SEM of $Zn_{1-x}Ni_xO$. (a) $Zn_{0.99}Ni_{0.01}O$. (b) $Zn_{0.98}Ni_{0.02}O$. (c) $Zn_{0.97}Ni_{0.03}O$. (d) $Zn_{0.96}Ni_{0.04}O$. (e) $Zn_{0.95}Ni_{0.05}O$. (f) $Zn_{0.9}Ni_{0.1}O$.

stitutional defect occurs in the hexagonal wurtzite structure. This results in the broadening of peaks in the XRD analysis, indicating a deviation from the original structure [47–51]. The band gap, electrical conductivity, and optical properties can be examined across different structures. Here, the photovoltaic properties are studied to understand the behavior of these structures. A semiconductor diode is a semiconductor device that consists of a p-type doped semiconductor (anode) on one side and an n-type semiconductor (cathode) on the other side. The cathode region has a large number of electrons, and the anode region has many holes. The connection of these two regions leads to the flow of electrons and the transfer of electrons to the holes in the anode. If photons with sufficient energy strike a semiconductor diode, electron-hole pairs are generated in the n and p regions within an area called the space-charge region (SCR).

Using this method, a photocurrent is generated that flows between the cathode and anode, and this is called a photodiode. In this article, zinc oxide is studied as a photodiode. This structure responds to ultraviolet light due to its around 4 eV band gap. Here, silicon serves as the p-type region and zinc oxide as the n-type region. The electrical circuit, which includes the diode, power supply, ammeter, and ultraviolet light, was set up as shown in Scheme 1. Ultraviolet light with a wavelength of 365 nm was selected, which is in the range of the maximum absorption wavelength for the zinc oxide structure. The dark current and the current under ultraviolet illumination were recorded [52–55].

Using the dark current and the light current, I_{Photo} is calculated using the following formula:

$$I_{Photo} = I_{UV} - I_{Dark} \tag{4}$$

The photocurrent was measured in the presence of ultraviolet light with a wavelength of 254 nm and an intensity of 268.27 W/cm^2. Then, the responsivity (R) and quantum efficiency (η) of each sample were calculated using formulas (5) and (6).

$$\eta = (I_{Photo}/q)/(P_{inc}/h\nu) \tag{5}$$

$$R = I_{Photo}/P_{inc} \tag{6}$$

As evident from the graphs and tables, both dark current and photocurrent under ultraviolet light are in the microampere range. Samples 1% and 5% exhibit higher dark current compared to samples 3% and 10%. In the 10% sample, the current passing through is less relative to the other samples, indicating from the IR and XRD analyses that, due to the high percentage of nickel substitution for zinc, nickel oxide forms instead of the intended substitutional defect structure, occupying the interstitial spaces within the lattice [56, 57]. Figure 5 shows the current-voltage characteristics of light passing through zinc oxide diodes doped with various percentages of nickel impurities. The highest current is observed for samples doped with 1%, 3%, 5%, and 10% nickel impurities, which is consistent with other characterization results. As observed in figure 6, the slope parameter of the ln (I_{Photo})-V curve is obtained, where a higher slope corresponds to a higher ideality factor. This curve exhibits a higher value for the 1% and 3% percentages, with the

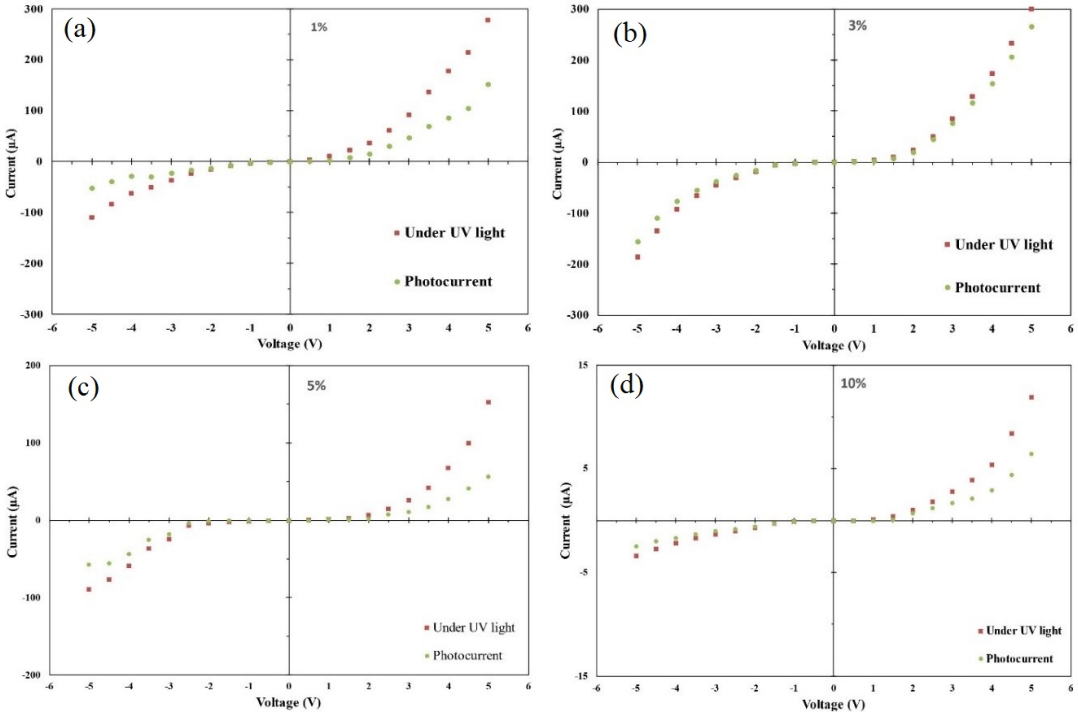

Figure 5. The current-voltage (IV) curves for each of samples. (a) $Zn_{0.99}Ni_{0.01}O$. (b) $Zn_{0.97}Ni_{0.03}O$. (c) $Zn_{0.95}Ni_{0.05}O$. (d) $Zn_{0.9}Ni_{0.1}O$.

sample at 3% showing the highest ideality factor.

By examining the current of diodes made without light exposure (dark current) and under ultraviolet light exposure in samples with different nickel percentages, it was found that $Zn_{0.97}Ni_{0.03}O$ and $Zn_{0.99}Ni_{0.01}O$ have the best characteristics. The superior performance of these samples can be attributed to their good crystal structure. It can also be concluded that nickel atoms at these percentages have effectively replaced zinc atoms [58–60].

In figure 6, the voltage-current diagram for samples with 1% and 3% nickel under different radiation is examined. As observed, the 1% sample has a better response at a wavelength of 385 nm, while the 3% sample has a better response at 365 nm. Both of these values fall within the ultraviolet spectrum range and within the lambda max range of zinc oxide. The 3% sample (according to UV analysis) has a larger energy gap compared to the 1% sample, which causes it to have a better response at this wavelength with higher energy. The diagram in figure 6 also confirms this.

Table 3. The responsivity and quantum efficiency of each sample.

$Zn_{(1-x)}Ni_xO$	R (A/W)	H	I_{ph}/I_d
X = 0	0.1	0.48	1.4
X = 0.01	0.13	0.62	0.16
X = 0.03	0.2	0.94	1.94
X = 0.05	0.1	0.51	0.24
X = 0.1	0.01	0.07	1.16

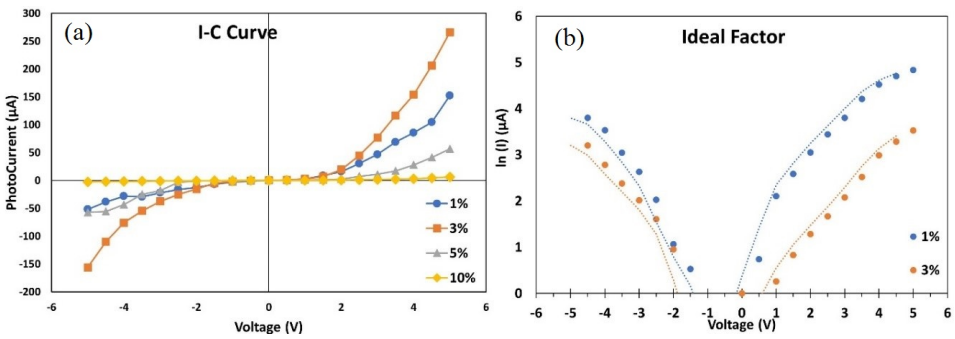

Figure 6. (a) I-C curve of 1%, 3%, 5% and 10% NZO. (b) Ideal factor of 1% and 3% NZO.

4. Conclusion

In this project, efforts were made to enhance the hexagonal zinc oxide structure using nickel atoms at concentrations of 1%, 3%, 5%, and 10%, and to investigate its band gap. XRD analysis showed that the zinc oxide structure, with the addition of nickel, reduced in size from 28 nm to 21 nm. This reduction could be due to the smaller size of nickel compared to zinc. The substituted nickel created defects, which led to peak broadening, and at 10% nickel concentration, the zinc oxide structure became saturated and a nickel oxide peak was observed. All structures were examined in UV, and it was observed from the energy-$\alpha h\nu$ plot that the structure experienced a blue shift with the addition of nickel, and the band gap increased. Analysis of the I_C plots revealed that the photocurrent of the 1% and 3% sample had great slope. The optimal cases for the current-voltage plots were found to be at 1% and 3%, with the ideal factor of the plot also being examined. This plot indicated that the NZO sample with 1% nickel could respond better and with higher energy at this wavelength. Therefore, among the ZnO structures with 1%, 3%, 5%, and 10% nickel, the 1% and 3% structures are expected to have the best performance.

Overall, the results indicate that nickel doping significantly modifies the structural and optical properties of ZnO. As nickel is added, the crystal size decreases, and defect formation increases, eventually leading to the formation of the NiO phase at higher concentrations. UV–Vis analysis reveals a clear blue shift and widening of the band gap due to doping. Photocurrent and current–voltage measurements reveal that the 1% and 3% samples perform noticeably better, with the 1% doped ZnO exhibiting the strongest response. Therefore, among all samples, the 1% and 3% Ni-doped ZnO structures demonstrate the most promising performance.

Authors Contribution
All authors have contributed equally to prepare the paper.

Availability of data and materials
The datasets generated during and/or analyzed during the current study are available from the corresponding author on reasonable request.

Conflict of interests
The authors declare that they have no known competing financial interests or personal relationships that could have appeared to influence the work reported in this paper.

References

[1] F. Ahmad and A. Maqsood. Structural, dielectric, impedance, complex modulus, and optical study of Ni-doped $Zn_{(1-x)}Ni_xO$ nanostructures at high temperatures. *Materials Research Express Journal*, , (2021).
DOI: https://doi.org/10.1088/2053-1591/ac2fcd.

[2] D. C. Joshi et al. Magnetic exchange interactions and dielectric studies of $Zn_{1-x}Ni_xO$–NiO composites. *Journal of Physics D: Applied Physics*, , (2017).
DOI: https://doi.org/10.1088/1361-6463/aa7826.

[3] M. Ahmed et al. Structural, optical and magnetic properties of dilute magnetic semiconductor of $Zn_{1-x}Ni_xO$ thin films for spintronic devices. *Journal of Ovonic Research*, , (2022).
DOI: https://doi.org/10.15251/JOR.2022.186.739.

[4] E. B. Buzok et al. The structural, optical, electrical and radiation shielding properties of Co-doped ZnO thin films. *Radiation Physics and Chemistry*, , (2024).
DOI: https://doi.org/10.1016/j.radphyschem.2024.111840.

[5] P. S. Menon et al. Influence of Defects on Optical and Nonlinear Optical Properties of Pristine and Nickel Doped Zinc Oxide Nanostructures. *SSRN*, , (2022).
DOI: https://doi.org/10.2139/ssrn.4023892.

[6] G. Demircan et al. Sol–gel synthesis of Si-ZnO, Ti-ZnO and Si-Ti-ZnO thin films: Impact of Si and Ti content on structural and optical properties. . *Materialstoday Communications*, , (2023).
DOI: https://doi.org/10.1016/j.mtcomm.2022.105234.

[7] J. Liu et al. Effects of Ni Doping Composition on the Physical and Electrical Properties of $Cu_{1-x}Ni_xO$ Thin-Film Transistors. . *IEEE Transactions on Electron Devices*, , (2022).
DOI: https://doi.org/10.1109/TED.2022.3145328.

[8] M. Zhang et al. A novel synthetic strategy towards NaCl-type $Ni_xCo_{1-x}O$ solid solution nanoplatelets encapsulated in N-doped carbon for enhanced lithium-ion storage. *Journal of Alloys and Compounds*, , (2021).
DOI: https://doi.org/10.1016/j.jallcom.2021.160694.

[9] X. Ma et al. Investigation on the structure and antibacterial performance of Ni-doped $Ti_{1-X}Ni_XO_2$ nanotubes. *Applied Surface Science*, , (2023).
DOI: https://doi.org/10.1016/j.apsusc.2023.158105.

[10] Z. Lu et al. Low content Ni-doped $BiFeO_3$ with efficient photo-Fenton degradation of tetracycline. *Optical Materials*, , (2022).
DOI: https://doi.org/10.1016/j.optmat.2022.113185.

[11] T. Abdel-Baset and S. El-Sayed. The effect of $Zn_{0.95}Ni_{0.05}O$ nanoparticles on the physical properties of polyvinyl chloride. *Polymer Bulletin*, .

[12] A. Singh et al. Synergistic effect of ZnO nanoparticles with Cu^{2+} doping on antibacterial and photocatalytic activity. *Inorganic Chemistry Communications*, , (2023).
DOI: https://doi.org/10.1016/j.inoche.2023.111425.

[13] S. Solaymany et al. Optical properties and surface dynamics analyses of homojunction and hetrojunction Q/ITO/ZnO/NZO and Q/ITO/ZnO/NiO thin films. *Results in Physics*, (2021).
DOI: https://doi.org/10.1016/j.rinp.2021.104679.

[14] S. Desgreniers. High-density phases of ZnO: Structural and compressive parameters. *Physical Review B*, , (1998).
DOI: https://doi.org/10.1103/PhysRevB.58.14102.

[15] J. Zhao et al. Structure and photocatalytic activity of Ni-doped ZnO nanorods. . *Materials Research Bulletin*, , (2011).
DOI: https://doi.org/10.1016/j.materresbull.2011.04.008.

[16] F. Yakuphanoglu, Y. Caglar, M. Caglar, and S. Ilican. ZnO/p-Si heterojunction photodiode by sol–gel deposition of nanostructure n-ZnO film on p-Si substrate. *Materials Science in Semiconductor Processing*, , (2010).
DOI: https://doi.org/10.1016/j.mssp.2010.05.005.

[17] M. Anujency et al. Enhancing the properties of ZnO nanorods by Ni doping via the hydrothermal method for photosensor applications. *Journal of Photochemistry and Photobiology A: Chemistry*, , (2024).
DOI: https://doi.org/10.1016/j.jphotochem.2023.115379.

[18] Al-Ariki et al. Synthesis and comparative study on the structural and optical properties of ZnO doped with Ni and Ag nanopowders fabricated by sol gel technique. *Scientific Reports*, , (2019).
DOI: https://doi.org/10.1038/s41598-021-91439-1.

[19] Y. Z. Zhu et al. Electronic structure and phase stability of MgO, ZnO, CdO, and related ternary alloys. *Physical Review B*, , (2008).
DOI: https://doi.org/10.1103/PhysRevB.77.245209.

[20] J. Z. Jiang et al. Structural stability in nanocrystalline ZnO. . *Europhysics Letters*, .

[21] N. P. Rini, N. I. Istiqomah, and E. Suharyadi. Enhancing photodegradation of methylene blue and reusability using CoO/ZnO composite nanoparticles. *Case Studies in Chemical and Environmental Engineering*, , (2023).
DOI: https://doi.org/10.1016/j.cscee.2023.100301.

[22] A. Jabr et al. The effect of liquid phase chemistry on the densification and strength of cold sintered ZnO. . *Journal of the European Ceramic Society*, , (2023).
DOI: https://doi.org/10.1016/j.jeurceramsoc.2022.11.071.

[23] S. M. Mustafa, A. A. Barzinjy, and A. H. Hamad. An environmentally friendly green synthesis of Co^{2+} and Mn^{2+} ion doped ZnO nanoparticles to improve solar cell efficiency. *Journal of Environmental Chemical Engineering*, , (2023).
DOI: https://doi.org/10.1016/j.jece.2023.109514.

[24] Z. Hajizadeh, R. Taheri-Ledari, and F. R. Asl. Identification and analytical methods. In Heterogeneous micro and nanoscale composites for the catalysis of organic reactions. *Micro and Nano Technologies*.

[25] F. R. Asl, F. Ganjali, and Z. Rashvandi. MOF Scaffolds Tunability and Flexibility. In: Maleki, A., Taheri-Ledari, R. (eds) Physicochemical Aspects of Metal-Organic Frameworks. *Engineering Materials*, Springer, Cham:101–111, (2023).
DOI: https://doi.org/10.1007/978-3-031-18675-2_8.

[26] Z. Rashvandi, F. R. Asl, and F. Ganjali. Coordination Chemistry of MOFs. In: Maleki, A., Taheri-Ledari, R. (eds) Physicochemical Aspects of Metal-Organic Frameworks. *Engineering Materials*, Springer, Cham:110–111, (2023).
DOI: https://doi.org/10.1007/978-3-031-18675-2_12.

[27] R. Elilarassi and G. Chandrasekaran. Synthesis, structural and optical characterization of Ni-doped ZnO nanoparticles. *Journal of Materials Science: Materials in Electronics.*, , (2011).
DOI: https://doi.org/10.1007/s10854-010-0206-8.

[28] S. Kumar et al. Electronic structure, magnetic and structural properties of Ni doped ZnO nanoparticles. *Materials Research Bulletin*, , (2014).
DOI: https://doi.org/10.1016/j.materresbull.2014.07.044.

[29] A. Omar et al. Investigation of morphological, structural and electronic transformation of PVDF and ZnO/rGO/PVDF hybrid membranes. *Optical and Quantum Electronics*, , (2023).
DOI: https://doi.org/10.1007/s11082-023-04663-6.

[30] A. Elbrolesy et al. Novel green synthesis of UV-sunscreen ZnO nanoparticles using solanum lycopersicum fruit extract and evaluation of their antibacterial and anticancer activity. *Journal of Inorganic and Organometallic Polymers and Materials*, , (2023).
DOI: https://doi.org/10.1007/s10904-023-02744-3.

[31] A. B. Djurišić and Y. H. Leung. Optical properties of ZnO nanostructures. . *Small*, , (2006).
DOI: https://doi.org/10.1002/smll.200600134.

[32] K. Liu, M. Sakurai, and M. Aono. ZnO-based ultraviolet photodetectors. *Sensors*, , (2010).
DOI: https://doi.org/10.3390/s100908604.

[33] G. Lakshminarayana and S. Buddhudu. Spectral analysis of Mn^{2+}, Co^{2+} and Ni^{2+}: B_2O_3–ZnO–PbO glasses. *Spectrochimica Acta Part A: Molecular and Biomolecular Spectroscopy*, , (2006).
DOI: https://doi.org/10.1016/j.saa.2005.05.013.

[34] S. Ahn et al. Determination of band gap energy (Eg) of $Cu_2ZnSnSe_4$ thin films: On the discrepancies of reported band gap values. *Applied Physics Letters*, , (2010).
DOI: https://doi.org/10.1063/1.3457172.

[35] G. Lakshminarayana et al. Physical, structural, thermal, and optical spectroscopy studies of TeO_2–B_2O_3–MoO_3–ZnO–R_2O (R = Li, Na, and K)/MO (M = Mg, Ca, and Pb) glasses. *Journal of Alloys and Compounds*, , (2017).
DOI: https://doi.org/10.1016/j.jallcom.2016.08.180.

[36] X. Cao et al. ZnO nanorods loading with fatty amine as composite PCMs device for efficient light-to-thermal and electro-to-thermal conversion. . *Journal of Colloid and Interface Science*, , (2023).
DOI: https://doi.org/10.1016/j.jcis.2022.09.032.

[37] K. H. Kim et al. A comparative study on the structural properties of ZnO and Ni-doped ZnO nanostructures. *Materials Letters*, , (2015).
DOI: https://doi.org/10.1021/acsami.2c20765.

[38] H. Yue et al. Flame-retardant and form-stable phase-change composites based on phytic acid/ZnO-decorated surface-carbonized delignified wood with superior solar-thermal conversion efficiency and improved thermal conductivity. *ACS Applied Materials & Interfaces*, , (2023).
DOI: https://doi.org/10.1039/D2RA07837F.

[39] B. Salem, Ben, et al. Synthesis and comparative study of the structural and optical properties of binary ZnO-based composites for environmental applications. *RSC Advances.*, , (2023).
DOI: https://doi.org/10.1039/D2RA07837F.

[40] T. Gruber et al. ZnMgO epilayers and ZnO–ZnMgO quantum wells for optoelectronic applications in the blue and UV spectral region. *Applied Physics Letters*, , (2004).
DOI: https://doi.org/10.1063/1.1767273.

[41] Y. Liu et al. Effects of Ni concentration on structural, magnetic and optical properties of Ni-doped ZnO nanoparticles. *Journal of Alloys and Compounds*, , (2014).
DOI: https://doi.org/10.1016/j.jallcom.2014.03.079.

[42] S. Fabbiyola et al. Optical and magnetic properties of Ni-doped ZnO nanoparticles. *Journal of Alloys and Compounds*, , (2017).
DOI: https://doi.org/10.1016/j.jallcom.2016.10.022.

[43] R. P. Pal Singh et al. Effect of Ni doping on structural, optical, and magnetic properties of Fe-doped ZnO nanoparticles. *Journal of Superconductivity and Novel Magnetism*, , (2015).
DOI: https://doi.org/10.1007/s10948-015-3183-6.

[44] W. Chehade et al. Synthesis and magneto-optical studies of novel $Ni_{0.5}Zn_{0.5}Fe_2O_4/Zn_{0.95}Co_{0.05}O$ nanocomposite as a candidate for photocatalytic applications. *Ceramics International*, , (2022).
DOI: https://doi.org/10.1016/j.ceramint.2021.09.209.

[45] A. B. Oshchepkov et al. Physical property modifications with transition metal doping in nanostructured Zn. *Journal of Physics: Conference Series*, , (2022).
DOI: https://doi.org/10.2139/ssrn.4023892.

[46] S. Pattanaik et al. Oxygen vacancy induced ferromagnetism in ball milled $Zn_{0.97}Ni_{0.03}O$: Confirmation through electron spin resonance. . *Materials Today: Proceedings*, , (2021).
DOI: https://doi.org/10.1016/j.matpr.2020.03.547.

[47] N. Üzar et al. Enhancement of structural, optical, electrical, optoelectronic and thermoelectric properties of ZnO thin film via Ni doping and Ni-B co-doping. . *Physica Scripta*, , (2024).
DOI: https://doi.org/10.1088/1402-4896/ad5873.

[48] R. Bhardwaj et al. Defect induced magnetism in Ni doped ZnO nanoparticles. . *AIP Publishing*, , (2020).
DOI: https://doi.org/10.1063/5.0001832.

[49] W. Wenjie et al. Synthesis of heteroatom-doped ZnO nanoparticles as an efficient visible light photocatalyst and its photoelectrochemical performance. *Indian Journal of Chemistry-Section A (IJCA)*, , (2020).

[50] A. F. Fathima and R. J. Mani. Impact of Transition metals (Fe, Co, Ni, Fe/Co, Fe/Au and Co/Au) doping on the magnetic properties of ZnO nanoparticles. *Applied Surface Science*, ISSN NO:1001-1749, (2022).

[51] S. Agrohiya et al. Nickel Doped Zinc Oxide Thin Films for Visible Blind Ultraviolet Photodetection Applications. *ECS Sensors Plus*, , (2022).
DOI: https://doi.org/10.1149/2754-2726/ac973f.

[52] P. GK et al. Effect of doping (with cobalt or nickel) and UV exposure on the antibacterial, anticancer, and ROS generation activities of zinc oxide nanoparticles. *Journal of Asian Ceramic Societies*, .

[53] A. Lins et al. Facile Synthesis of Ni-Doped ZnO Nanoparticles Using Cashew Gum: Investigation of the Structural, Optical, and Photocatalytic Properties. *Molecules*, , (2023).
DOI: https://doi.org/10.3390/molecules28237772.

[54] I. Zharchenko et al. Investigating hot carrier effects in GaAs PN diodes under pulsed laser irradiation. *Materials of international scientific and technical conference "Laser technologies. Lasers and their application (LTLA 2023)"*, , (2023).

[55] S. Ašmontas et al. Laser induced photoresponse in perovskite solar cells. *Materials of international scientific and technical conference "Laser technologies. Lasers and their application (LTLA 2023)"*., , (2023).
DOI: https://doi.org/10.15251/JOR.2022.186.739.

[56] A. Aridi et al. Enhanced adsorption performance of magnetic $Ni_{0.5}Zn_{0.5}Fe_2O_4/Zn_{0.95}Co_{0.05}O$ nanocomposites for the removal of malachite green dye. *Environmental Science and Pollution Research*, , (2023).
DOI: https://doi.org/10.1007/s11356-023-26608-y.

[57] N. Rizvi, A. Rehman, and M. T. Khan. To Study the Structural, Optical and Magnetic Properties of Ni-Fe Doped ZnO Diluted Magnetic Semiconductors. . *NUST Journal of Engineering Sciences*, , (2022).
DOI: https://doi.org/10.24949/njes.v15i1.678.

[58] T. G. Reda et al. Potential Antibacterial Applications and Synthesis, Structural, Magnetic, Optical, and Dielectric Characterization of Nickel-Substituted Cobalt Ferrite Nanoparticles. . *Research Square*, , (2024).
DOI: https://doi.org/10.21203/rs.3.rs-4512246/v1.

[59] M. W. Ibrahim et al. Mesoporous aluminosilicate materials supported zinc oxide photocatalytic degradation of pharmaceutical pollutants. . *Desalination and Water Treatment*, , (2024).
DOI: https://doi.org/10.1016/j.dwt.2024.100588.

[60] A. Zukuls et al. Degenerated ZnO Nanocrystals: Synthesis, Properties and Applications. . Papildus informācija, (2021).
DOI: https://doi.org/10.7250/9789934225871.